1D study of radiation-dominated implosion of a cylindrical tungsten plasma column ‡

M M Basko[1,2], P V Sasorov[1], M Murakami[2], V G Novikov[3] and A S Grushin[3]

[1] Alikhanov Institute for Theoretical and Experimental Physics, Moscow, Russia
[2] Institute of Laser Engineering, Osaka University, Suita, Osaka 565-0871, Japan
[3] Keldysh Institute of Applied Mathematics, Moscow, Russia

E-mail: basko@itep.ru

Abstract. Spectral properties of the x-ray pulses, generated by perfectly uniform cylindrical implosions of tungsten plasma with parameters typical of wire array z-pinches, are investigated under the simplifying assumption that the final stage of the kinetic-to-radiant energy conversion is not affected by the magnetic field. The x-ray emission is shown to be generated within a narrow (sub-micron) radiation-dominated stagnation shock front with a "supercritical" amplitude. The structure of the stagnation shock is investigated by using two independent radiation-hydrodynamics codes, and by constructing an approximate analytical model. The x-ray spectra are calculated for two values of the plasma column mass, 0.3 mg cm^{-1} and 6 mg cm^{-1}, with a newly developed two-dimensional radiation-hydrodynamics code RALEF-2D. The hard component of the spectrum (with a blackbody-fit temperature of 0.5–0.6 keV for the 6-mg cm^{-1} mass) originates from a narrow peak of the electron temperature inside the stagnation shock. The softer main component emerges from an extended halo, where the primary shock radiation is reemitted by colder layers of the imploding plasma. Our calculated x-ray spectrum for the 6-mg cm^{-1} tungsten column agrees well with the published Sandia experimental data (Foord *et al* 2004 *Phys. Rev. Lett.* **93**, 055002).

‡ This is an author-created, un-copyedited version of an article published in *Plasma Phys. Control. Fusion*, **54** (2012) 055003. IOP Publishing Ltd is not responsible for any errors or omissions in this version of the manuscript or any version derived from it. The Version of Record is available online at doi:10.1088/0741-3335/54/5/055003

1. Introduction

Wire array z-pinches proved to be one of the most efficient and practical way to generate multi-terawatt pulses of quasi-thermal x-rays with duration of a few nanoseconds [1, 2]. This implies reach potential for many applications, in particular, as an attractive driver for inertial confinement fusion (ICF) [3, 4]. From theoretical point of view, the wire array z-pinch is a complex physical phenomenon: its adequate modelling requires sophisticated multi-dimensional magnetohydrodynamic (MHD) simulations of a complex plasma-metal configuration, whose dynamics at a later stage is strongly influenced by radiative processes [5, 6, 7].

The focus of this paper is on a single specific aspect of this phenomenon, namely, on the physics of conversion of the kinetic energy of the imploding pinch into the emerging pulse of x-rays. We solve an idealized one-dimensional (1D) problem where a high-velocity cylindrical implosion of tungsten plasma is stopped according to the laws of pure radiation hydrodynamics, with a possible role of MHD effects neglected. We believe that, despite a seemingly oversimplified statement of the problem, thus obtained results will prove to be useful for interpretation and subsequent modelling of the x-ray pulses and their spectra in wire array z-pinches optimized for maximum x-ray power. The emission that we calculate should primarily refer to the main part of the observed pulses, i.e. to the x-ray flux in a narrow time window around the peak of the x-ray power with the full width at half maximum (FWHM) roughly equal to its rise time ($\simeq 5$ ns in a typical 18–19 MA shot on the Z machine at Sandia [8]). Note that thus defined main pulse may only contain about 50% of the total x-ray emitted energy [8].

Our analysis is based on the assumption that practically all the energy radiated in the main pulse originates from the kinetic energy of the imploding plasma. Such a premise is corroborated by the latest 3D MHD simulations of imploding wire arrays [7]. To simplify the treatment, we do not consider the acceleration stage of the plasma implosion and start with an initial state at maximum implosion velocity. Hence, we do not have to consider the $\mathbf{j} \times \mathbf{B}$ force which drives the implosion (i.e. accelerates the plasma but generates little entropy) because the entire kinetic energy of the implosion can be simply prescribed at the initial state. The resistive (Ohmic) dissipation of the electromagnetic energy was found to be negligible anyway [7]. More difficult is to justify our neglect of the MHD effects at the final stage of plasma deceleration and x-ray generation. Although some additional arguments to this point are given in the summary, we must admit that full clarification of this issue remains for future work.

Under the assumptions made, we find that the kinetic energy of the implosion is converted into radiation when the plasma passes through a stagnation shock near the axis. In wire arrays with powerful x-ray emission the stagnation shock falls into the category of "supercritical" radiation-dominated (RD) shock fronts [9]. Such fronts are characterized by an extremely small width, and their thermal structure is primarily controlled by emission and transport of thermal radiation. Our results imply that adequate modelling of the temperature and density profiles across the narrow stagnation

shock front is key to understanding the x-ray spectra emitted by powerful wire array z-pinches.

The paper is organized as follows. In section 2 we describe the initial state of the simulated plasma flow; section 3 elaborates on the two numerical codes used for simulations. Section 4 is devoted to the detailed analysis of the stagnation shock structure: we construct an approximate analytical model, which is corroborated by numerical simulations and allows simple evaluation of the key plasma parameters in the shock front. In section 5 we present the calculated spectra of the x-ray pulses, radial profiles of the spectral optical depth, spectral x-ray images of the plasma column. The emergent x-ray spectra have been calculated for two values of the linear pinch mass, 0.3 mg cm^{-1} and 6 mg cm^{-1}, by employing a newly developed two-dimensional (2D) radiation-hydrodynamics code RALEF-2D.

2. Initial configuration

We choose the simplest initial configuration that allows reproduction of the principal characteristics of the observed x-ray pulses. We start with a cylindrical shell of tungsten plasma, converging onto the pinch axis $r = 0$ with an initial implosion velocity $u(0, r) = -U_0$ ($U_0 > 0$) constant over the shell mass. The imploding shell is supposed to have sharp boundaries at $r = r_1(t)$ and $r = r_1(t) + \Delta_0$. Once the radial velocity peaks at U_0, the implosion can be treated as "cold" in the sense that the plasma internal energy is small compared to its kinetic energy, the role of pressure forces is negligible, and the shell thickness freezes at a constant value Δ_0. We begin our simulations at time $t = 0$ when the inner shell edge arrives upon the axis, i.e. when $r_1 = r_1(0) = 0$.

The density distribution across the imploding shell is assumed to have been uniform at earlier times, when the inner shell radius was $r_1(t) \gg \Delta_0$. In a cold implosion this leads to the initial radial density profile of the form

$$\rho_0(r) = \left(\frac{m_0}{2\pi\Delta_0}\right)\frac{1}{r}, \tag{1}$$

where m_0 is the linear (per unit cylinder length) mass of the shell.

In this paper we present simulations for two cases, namely, case A (referring to the 5-MA Angara-5-1 machine in Troitsk, Russia) and case Z (referring to the 20-MA Z accelerator at Sandia, USA). In both cases we used the same values of the implosion velocity and shell thickness,

$$U_0 = 400 \text{ km s}^{-1} = 4 \times 10^7 \text{ cm s}^{-1}, \qquad \Delta_0 = 2 \text{ mm}. \tag{2}$$

The peak implosion velocity of 400 km s^{-1} has been inferred from the experimental data for optimized shots on both the Angara-5-1 [10] and the Z machines [11], and confirmed by numerical simulations [5, 7]. For the given U_0, the shell thickness Δ_0 is set equal to 2 mm to conform with the observed x-ray pulse duration of 5 ns (FWHM) [1, 2, 12, 13]. Note that if, in addition, we assumed a 100% instantaneous conversion of the kinetic

energy into x-rays, we would obtain a rectangular x-ray pulse of duration

$$t_0 = \frac{\Delta_0}{U_0} = 5 \text{ ns} \tag{3}$$

with the top nominal power

$$P_0 = \frac{m_0 U_0^3}{2\Delta_0} \tag{4}$$

(per unit cylinder length).

Thus, the only parameter that differs between the cases A and Z is the linear mass m_0 of the imploding shell. In simulations we used the values

$$m_0 = \begin{cases} 0.3 \text{ mg cm}^{-1}, & \text{case A}, \\ 6.0 \text{ mg cm}^{-1}, & \text{case Z}, \end{cases} \tag{5}$$

which are representative of a series of optimized (with respect to the peak power and total energy of the x-ray pulse) experiments at a 3 MA current level on Angara-5-1 [13], and at a 19 MA current level on Z [8]. These two values of m_0 correspond to the nominal powers

$$P_0 = \begin{cases} 4.8 \text{ TW cm}^{-1}, & \text{case A}, \\ 96 \text{ TW cm}^{-1}, & \text{case Z}, \end{cases} \tag{6}$$

which are close to the peak x-ray powers measured in the corresponding experiments.

The final parameter needed to fully specify the initial state is the initial temperature T_0 of the imploding plasma. In both cases we used the same value $T_0 = 20$ eV, which falls in the 10–30 eV range inferred from the theory of plasma ablation in multi-wire arrays [14, 15, 16] and confirmed by direct MHD simulations of the wire-corona plasma [5]. The sound velocity in a 20-eV tungsten plasma, $c_\mathrm{s} \approx (0.5\text{–}1.0) \times 10^6$ cm s^{-1}, implies implosion Mach numbers as high as $U_0/c_\mathrm{s} \approx 40\text{–}80$ — which fully justifies the above assumption of a cold implosion.

3. The DEIRA and the RALEF-2D codes

Numerical simulations have been performed with two numerical codes that are based on different numerical techniques and include fully independent models of all physical processes, namely, with a 1D three-temperature (3T) code DEIRA [17, 18], and a 2D radiation-hydrodynamics code RALEF-2D [19]. Because of strongly differing physical models and numerical capabilities, the results obtained with these two codes are to a large extent complimentary to one another. The 2D RALEF code was used to simulate our 1D problem simply because we had no adequate 1D code with spectral radiation transport at hand.

3.1. The DEIRA code

The 1D 3T DEIRA code was originally written to simulate ICF targets [17]. It is based on one-fluid Lagrangian hydrodynamics with a tensor version of the Richtmyer

artificial viscosity and different electron, T_e, and ion, T_i, temperatures. Included also are the electron and the ion thermal conduction, as well as the ion physical viscosity. The model for the electron and the ion conduction coefficients is based on the Spitzer formula, modified in such a way as to match the experimental data near normal conditions [18]. The equation of state is based on the average ion model [20], which accounts for both the thermal and the pressure ionization at high temperatures and/or densities, as well as for realistic properties of materials near normal conditions.

Energy transport by thermal radiation is described by a separate diffusion equation for the radiative energy density $\rho\epsilon_\mathrm{r} = a_\mathrm{S}T_\mathrm{r}^4$, expressed in terms of a separate radiation temperature T_r; here a_S is the Stefan constant. The energy relaxation between the electrons and the radiation is expressed in terms of the Planckian mean absorption coefficient k_Pl, while the radiation diffusion coefficient is coupled to the Rosseland mean k_R. The absorption coefficients k_Pl and k_R are evaluated in-line as a combined contribution from the free-free, bound-free and bound-bound electron transitions plus the Thomson scattering. For the bound-bound and bound-free transitions, an approximate model, based on the sum rule for the dipole oscillator strengths [21], is used. At every $(n+1)$-th time step the subset of the three discretized energy equations is solved in a fully implicit manner by linearizing with respect to the three unknown temperatures T_e^{n+1}, T_i^{n+1} and T_r^{n+1} — i.e. by expanding any temperature-dependent term $E(T^{n+1})$ as $E(T^{n+1}) = E(T^n)+E'_T(T^{n+1}-T^n)$, where $E(T^n)$ and $E'_T = \partial E/\partial T$ are known from the previous n-th step, and solving the resulting system of linear equations with respect to T_e^{n+1}, T_i^{n+1} and T_r^{n+1}.

3.2. The RALEF-2D code

RALEF-2D (Radiative Arbitrary Lagrangian-Eulerian Fluid dynamics in two Dimensions) is a new radiation-hydrodynamics code, whose development is still underway [19]. Its hydrodynamics module is based on the upgraded version of the CAVEAT hydrodynamics package [22]. The one-fluid one-temperature hydrodynamic equations are solved in two spatial dimensions [in either Cartesian (x, y) or axisymmetric (r, z) coordinates] on a multi-block structured quadrilateral grid by a second-order Godunov-type numerical method. An important ingredient is the rezoning-remapping algorithm within the Arbitrary Lagrangian-Eulerian (ALE) approach to numerical hydrodynamics. The original mesh rezoning scheme, based on the Winslow equipotential method [23], proved to be quite efficient for the interior of the computational domain, if the mesh is smooth along the boundaries; in RALEF, a new high-order method for rezoning block boundaries has been implemented to this end.

New numerical algorithms for thermal conduction and radiation transport have been developed within the unified symmetric semi-implicit approach [24] with respect to time discretization. The algorithm for thermal conduction is a conservative, second-order accurate symmetric scheme on a 9-point stencil [25], where thermal fluxes through the four edges of every quadrilateral mesh cell are calculated by using the temperature

values in this same cell and its eight nearest neighbours. Radiation energy transport is described by the quasi-static transfer equation

$$\mathbf{\Omega} \cdot \nabla I_\nu = k_\nu \left(B_\nu - I_\nu \right) \tag{7}$$

for the spectral radiation intensity $I_\nu = I_\nu(t, \mathbf{x}, \mathbf{\Omega})$; the term $c^{-1} \partial I_\nu / \partial t$, where c is the speed of light, is neglected. A non-trivial issue for spatial discretization of equation (7) together with the radiative heating term

$$Q_\mathrm{r} = -\operatorname{div} \int_0^\infty d\nu \int_{4\pi} I_\nu \, \mathbf{\Omega} \, d\mathbf{\Omega} \tag{8}$$

in the hydrodynamic energy equation, is correct reproduction of the diffusion limit on distorted non-orthogonal grids [26]. In our scheme, we use the classical S_n method to treat the angular dependence of the radiation intensity $I_\nu(t, \mathbf{x}, \mathbf{\Omega})$, and the method of short characteristics [27] to integrate equation (7). The latter has a decisive advantage that every grid cell automatically receives the same number of light rays. Correct transition to the diffusion limit is achieved by special combination of the first- and second-order interpolation schemes in the finite-difference approximations to equations (7) and (8). More details on the numerical scheme for radiation transfer are to be published elsewhere.

In the present work we used the equation of state (EOS), thermal conductivity and spectral opacities provided by the THERMOS code [28], which has been developed at the Keldysh Institute of Applied Mathematics (Moscow). The spectral opacities are generated by solving the Hatree-Fock-Slater equations for plasma ions under the assumption of equilibrium level population. In combination with the equilibrium Planckian intensity B_ν, used in (7) as the source function, the latter means that we treat radiation transport in the approximation of local thermodynamic equilibrium (LTE) — which is justified for relatively dense and optically thick plasmas considered here.

The transfer equation (7) is solved numerically for a selected number of discrete spectral groups $[\nu_j, \nu_{j+1}]$, with the original THERMOS absorption coefficients k_ν averaged inside each group j by using the Planckian weight function. Two different sets of frequency groups are prepared for each code run: the primary set with a smaller number of groups (either 8 or 32 in the present simulations) is used at every time step in a joint loop with the hydrodynamic module, while the secondary (diagnostics) set with a larger number of groups (200 in the present simulations) is used in the post-processor regime at selected times to generate the desired spectral output data. An example of the spectral dependence of k_ν, provided by the THERMOS code for a tungsten plasma at $\rho = 0.01$ g cm^{-3}, $T = 250$ eV, is shown in figure 1 together with the corresponding group averages used in the RALEF simulations.

3.3. Numerical setup for the RALEF simulations

To test the sensitivity of the results with respect to spectral radiation transport, we did our simulations with two selections for the primary set of frequency groups, namely,

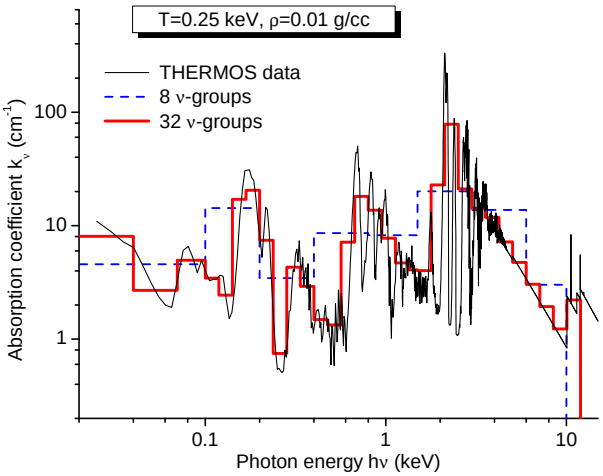

Figure 1. (Colour online) Spectral absorption coefficient k_ν [cm^{-1}] of tungsten at $\rho = 0.01$ g cm^{-3}, $T = 250$ eV used in the present simulations: shown are the original data from the THERMOS code (thin solid curve) together with the group-averaged values for 8 (dashed) and 32 (thick solid) selected spectral groups.

- with 8 groups delimited by the photon energies

$$h\nu_j = 10^{-3},\ 0.1,\ 0.2,\ 0.4,\ 0.8,\ 1.5,\ 3.0,\ 6.0,\ 10.0\ \text{keV}, \tag{9}$$

- and with 32 groups delimited by

$$\begin{aligned} h\nu_j = 10^{-3},\ & 0.02,\ 0.04,\ 0.07,\ 0.1,\ 0.119,\ 0.1414,\\ & 0.168,\ 0.20,\ 0.238,\ 0.2828,\ 0.336,\ 0.4,\ 0.476,\\ & 0.5656,\ 0.672,\ 0.8,\ 0.952,\ 1.1312,\ 1.344,\ 1.5,\\ & 1.785,\ 2.121,\ 2.52,\ 3.0,\ 3.57,\ 4.242,\ 5.04,\\ & 6.0,\ 7.14,\ 8.484,\ 10.08,\ 12.0\ \text{keV}. \end{aligned} \tag{10}$$

The 200 spectral groups of the secondary (diagnostics) frequency set were equally spaced along $\ln(h\nu)$ between $h\nu_1 = 0.01$ keV and $h\nu_{201} = 10$ keV. The angular dependence of the radiation intensity was calculated with the S_{14} method, which offers 28 discrete ray directions per octant.

The simulated region occupied one quadrant $0 \le \phi \le 90°$ of the azimuth angle ϕ with reflective boundaries along the x- and y-axes. Near the geometrical centre $x = y = 0$, a rigid transparent wall was placed at $r = r_0 = 10$ μm with the boundary conditions of $u(t, r_0) = 0$ and zero thermal flux. Thermal radiation passed freely through this cylindrical wall and was reflected by the two perpendicular reflective boundaries. Two variants of the initial polar mesh were used: a $n_\phi \times n_\mathrm{r} = 50 \times 250$ mesh in case A, and a $n_\phi \times n_\mathrm{r} = 60 \times 600$ mesh in case Z. At the outer boundary (initially at $r = R_0 = 2$ mm), the boundary conditions of zero external pressure and zero incident radiation flux were applied.

4. Stagnation shock

4.1. General picture

Upon arrival at the axis, the imploding plasma comes to a halt passing through a stagnation shock. In our situation the specific nature of this shock is defined by the dominant role of the radiant energy exchange. A detailed general analysis of the structure of such RD shock waves is given in [9, Ch. VII]. Perhaps the most salient feature of an RD shock with a supercritical amplitude is a very narrow local peak of matter temperature immediately behind the density jump [9]. This temperature peak manifests itself as a hair-thin bright circle at $r = r_s \approx 43$ μm on the 2D temperature plot in figure 2.

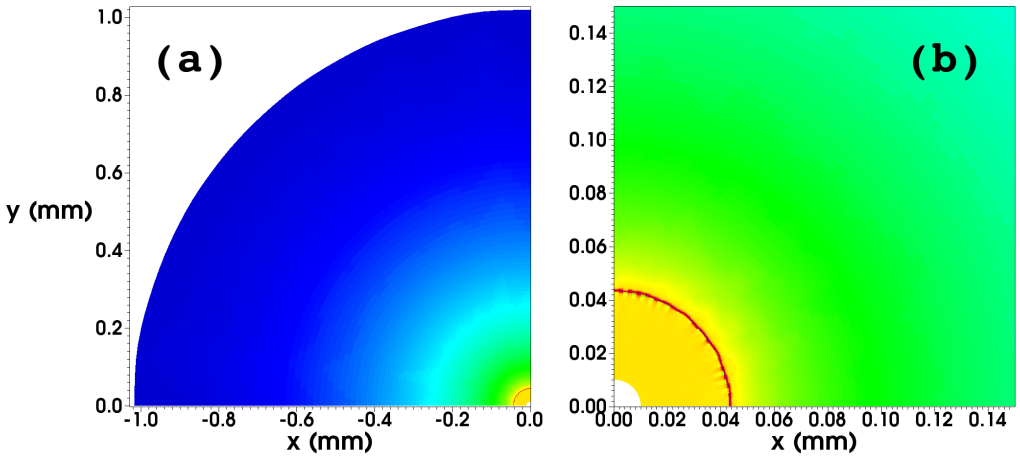

Figure 2. (Colour) 2D contour maps of matter temperature at $t = 3$ ns in case A (as calculated with the RALEF code): frame (b) is a blow up of the central part of the full view (a). Colour represents matter temperature T. A thin dark-red circle at $r = 43$ μm marks the position of the stagnation shock.

To achieve an adequate numerical resolution of the RD shock front, one needs a very fine grid that can only be afforded in 1D simulations. Figures 3 and 4 show the density and temperature profiles across the stagnation shock at $t = 3$ ns as calculated with the 1D DEIRA code on a uniform Lagrangian mesh with 20 000 mass intervals. If we define the shock-front width Δr_s to be the FWHM of the hump on the T_e profile, we obtain $\Delta r_s = 0.5$ μm in case A, and $\Delta r_s = 0.3$ μm in case Z. The peak values of the electron temperature are calculated to be $T_{ep} = 0.35$ keV in case A, and $T_{ep} = 0.54$ keV in case Z.

In a model where one distinguishes between the electron and the ion temperatures but ignores viscosity and ion heat conduction, the shock front has a discontinuity in the density and T_i profiles. In figures 3 and 4 this discontinuity is smeared out (roughly over 3 mesh cells) by the artificial Richtmyer-type viscosity, present in the DEIRA code. The electron temperature T_e, which exhibits a prominent hump over the virtually constant radiation temperature T_r, is continuous because the electron thermal conduction plays

a significant role. Clearly, the plasma inside the dense part of the T_e hump must be intensely loosing energy via thermal radiation.

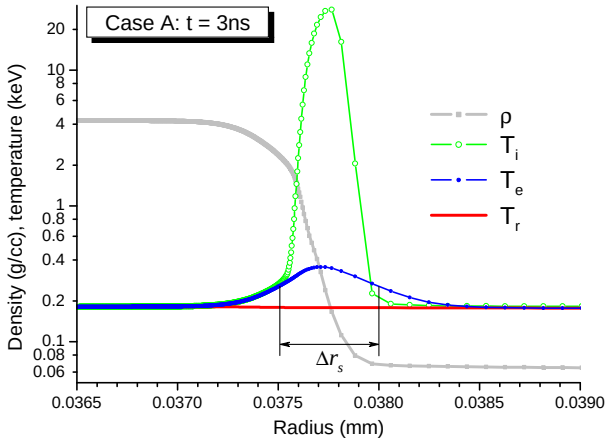

Figure 3. (Colour online) Density and temperature profiles across the stagnation shock in case A as calculated with the DEIRA code for $t = 3$ ns. The effective width Δr_s of the shock front is defined as the FWHM of the local peak of the electron temperature T_e. The velocity profile in the shock frame can be easily restored from the density plot and the condition $\rho v = constant$, which is quite accurately observed in the displayed region.

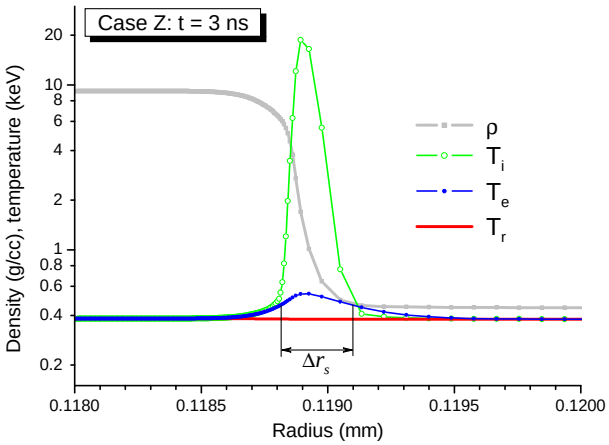

Figure 4. (Colour online) Same as figure 3 but for case Z.

Figures 3 and 4 demonstrate prominent peaks of the ion temperature T_i, whose maximum values $T_{ip} \approx 20$ keV significantly exceed the peak electron temperature T_{ep}. This fact, however, turns out to be rather insignificant for the radiative properties of the imploding plasma. Indeed, if we assume that the kinetic energy of the infalling plasma is fully converted into the ion thermal energy within a density-temperature discontinuity and ignore the plasma preheating before the shock, we calculate an after-shock ion temperature of

$$T_{i+} = \frac{\gamma - 1}{2} m_i U_0^2 = \frac{1}{3} m_i U_0^2 = 100 \text{ keV}; \tag{11}$$

here $\gamma = 5/3$ is the adiabatic index of the ideal gas of plasma ions, m_i is the mass of a tungsten ion. The DEIRA simulations demonstrate much lower peak ion temperatures because the preheating of the pre-shock plasma electrons, followed by their adiabatic compression in the density jump, consumes a large portion of the initial ion kinetic energy (in a collisionless manner via ambipolar electric fields). As a consequence, even before the collisional electron-ion relaxation sets in, the post-shock electrons with a temperature of $T_\mathrm{e} \approx 0.4$ keV already contain almost twice as much energy as the post-shock ions with a temperature of $T_\mathrm{i} \approx 20$ keV. Hence, the subsequent collisional electron-ion relaxation does not significantly affect the T_e profile. This fact has also been verified directly: having performed additional DEIRA runs in the 2T mode (i.e. assuming $T_\mathrm{e} = T_\mathrm{i} = T$), we obtained T profiles that were hardly distinguishable from the T_e profiles in figures 3 and 4 (the difference between the peak values T_p and T_ep did not exceed 3%). Thus, the approximation of a single matter temperature $T = T_\mathrm{e} = T_\mathrm{i}$, used in the 2D RALEF code, is well justified for our problem.

4.2. Analytical model

The theory of RD shock fronts, developed by Yu. P. Raizer [29] and described in his book with Ya. B. Zel'dovich [9], applies to planar shock waves in an infinite medium, which eventually absorbs all the emitted photons. We, in contrast, are dealing with a finite plasma mass, which lets out practically all the radiation flux generated at the shock front. In addition, the electron heat conduction, ignored in Raizer's treatment, plays an important role in formation of the temperature profile across the shock front. Hence, we have to reconsider certain key aspects of the Raizer's theory in order to obtain an adequate model for the stagnation shock in imploding z-pinch plasma.

4.2.1. General relationships To construct an analytical model of the plasma flow, we have to make certain simplifying assumptions. First of all, we assume a single temperature T for ions and electrons and employ the ideal-gas equation of state in the form

$$p = A\rho T, \qquad \epsilon = \frac{A}{\gamma - 1}\, T, \tag{12}$$

where p is the pressure, ϵ is the mass-specific internal energy, and A and $\gamma > 1$ are constants. The thermodynamic properties of the tungsten plasma in the relevant range of temperatures and densities are reasonably well reproduced with

$$A = \begin{cases} 13 \text{ MJ g}^{-1} \text{ keV}^{-1} & \text{in case A,} \\ 20 \text{ MJ g}^{-1} \text{ keV}^{-1} & \text{in case Z,} \end{cases} \tag{13}$$

$$\gamma = \begin{cases} 1.29 & \text{in case A,} \\ 1.33 & \text{in case Z.} \end{cases} \tag{14}$$

These values of A and γ have been obtained by substituting the values of p and ϵ, calculated with the THERMOS code [28] for the typical density ρ and temperature T in the post-shock state, into the relationships (12). If the post-shock state is a priori

poorly known, an iterative procedure for determination of A and γ may be needed to achieve better accuracy of the analytical estimates.

At each time t the entire plasma flow can be divided into three zones: the inner stagnation zone (the compressed core) at $0 < r < r_\mathrm{s}$ behind the shock front, the shock front itself confined to a narrow layer around $r = r_\mathrm{s}$, and the outer layer of the unshocked infalling material at $r > r_\mathrm{s}$. In the stagnation zone the plasma velocity is small compared to U_0, while the temperature and density are practically uniform and have the final post-shock values of $T = T_1 = T_1(t)$, $\rho = \rho_1 = \rho_1(t)$. Because the plasma flow in the stagnation zone is subsonic, pressure is rapidly equalized by hydrodynamics, while temperature is equalized by efficient radiative heat conduction; note that typical values of the mean Rosseland optical thickness of the stagnant core lie in the range $\tau_\mathrm{c,Ros} \simeq 10$–$100$. Numerical simulations confirm that spatial density and temperature variations across the compressed core do not exceed a few percent.

We identify the shock radius $r_\mathrm{s} = r_\mathrm{s}(t)$ with the density (and velocity) discontinuity, which is always present in sufficiently strong shocks once a zero physical viscosity is assumed [9]. Here and below the term "shock front" is applied to a narrow layer with an effective width of $\Delta r_\mathrm{s} \ll r_\mathrm{s}$, where the matter (electron) temperature T exhibits a noticeable hump above the radiation temperature T_r; see figures 3 and 4. Outside the shock front at $r > r_\mathrm{s}$ lies a broad preheating zone, which extends virtually over the entire unshocked material and has a width well in excess of the shock radius r_s. In this region the infalling plasma is preheated due to interaction with the outgoing radiation; in the process, it is also partially decelerated and compressed.

To analyze the structure of the shock front, we use the three basic conservation laws

$$\rho v \equiv -j = \mathit{constant}, \tag{15}$$

$$p + \rho v^2 = \mathit{constant}, \tag{16}$$

$$\rho v \left(w + \frac{v^2}{2} \right) + S_\mathrm{e} + S_\mathrm{r} = \mathit{constant}, \tag{17}$$

governing a steady-state hydrodynamic flow without viscosity across a planar shock front [9]; here

$$w = \epsilon + \frac{p}{\rho} = \frac{\gamma A}{\gamma - 1}\, T \tag{18}$$

is the specific enthalpy, S_e and S_r are the energy fluxes due, respectively, to the electron thermal conduction and radiation transport. Equations (15)–(17) are written in the reference frame comoving with the shock front: in this frame the plasma velocity $v < 0$. To avoid confusion, we use symbol "v" for the plasma velocity in the shock frame, and symbol "u" for the plasma velocity in the laboratory frame. The velocity of the shock front in the laboratory frame is $u_\mathrm{s} = \mathrm{d}r_\mathrm{s}/\mathrm{d}t$.

On the global scale, the plasma flow that we investigate is non-steady and cylindrically convergent. However, when analyzing the spatial profiles of basic variables

across a narrow shock front at $|r - r_s| \simeq \Delta r_s \ll r_s$, application of the quasi-steady-state planar relationships (15)–(17) is fully justified. Indeed, the values of the fluxes on the right-hand sides of Eqs. (15)–(17) change relatively slowly in time, on a time scale of Δ_0/U_0 (a few nanoseconds). Because this time scale is much longer than the time $\Delta r_s/U_0$ (on the order of several picoseconds in our case) in which any fluid element passes through the shock front, we can safely use the steady-state approximation provided that the slowly varying fluxes of mass, momentum and energy in Eqs. (15)–(17) are correctly evaluated from the global flow picture. Also, once $\Delta r_s \ll r_s$, the narrow shock front can be treated as locally planar.

4.2.2. Parameters of the stagnant core We begin by deriving a system of equations, from which the parameters of the stagnant plasma core can be evaluated. Although the sought-for quantities formally depend on time t, time appears only as a parameter in the final equations. The final post-shock plasma state can be determined in the approximation of zero thermal conduction, which redistributes energy only locally, in the immediate vicinity of the shock front. Without thermal conduction, the density and the temperature should have profiles shown qualitatively in figure 5: the density jump from $\rho = \rho_-$ to $\rho = \rho_+$ is accompanied by the jump in temperature from $T = T_-$ to $T = T_+$. Immediately behind (in the downstream direction) the temperature peak T_+ lies a narrow relaxation zone to the final state (ρ_1, T_1), where the excess thermal energy between the T_+ and T_1 states is rapidly radiated away.

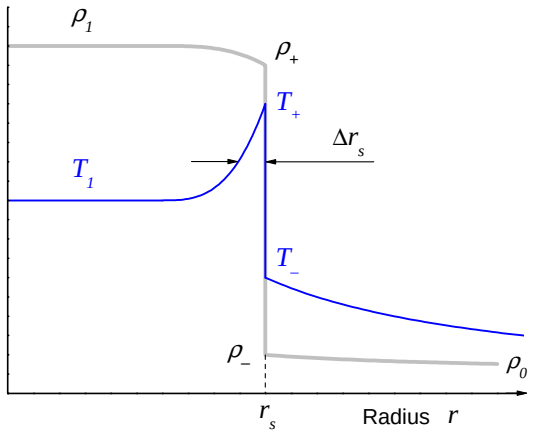

Figure 5. (Colour online) Schematic view of the density, ρ, and temperature, T, profiles across an RD shock front in the approximation of zero viscosity and heat conduction. The relaxation zones before and after the density jump are due to energy transport by radiation.

As was rigorously proven by Ya. B. Zel'dovich [30], the preheating temperature T_- at the entrance into the density jump can never exceed T_1. How does T_- compare with T_1, depends on whether the RD shock is subcritical or supercritical. A critical

amplitude of an RD shock front corresponds to the condition [29]

$$\sigma T_1^4 = \rho_1 u_\mathrm{s} \epsilon_1 \approx \rho_0 U_0 \frac{A T_1}{\gamma - 1} \tag{19}$$

that the one-sided radiation energy flux σT_1^4 becomes comparable to the hydrodynamic energy flux $\rho_1 u_\mathrm{s} \epsilon_1$ behind the shock front; here σ is the Stefan-Boltzmann constant. In our case the RD shock becomes supercritical when the post-shock temperature exceeds the critical value of

$$T_{1,cr} \approx 0.3\, \rho_{0,\mathrm{g/cc}}^{1/3} \text{ keV}, \tag{20}$$

where $\rho_{0,\mathrm{g/cc}}$ is the initial density (1) at $r = r_\mathrm{s}$ in g cm^{-3}. A posteriori, having calculated T_1 and r_s from the equations given below, we verify that our shock fronts are supercritical. As shown by Yu. P. Raizer [29], when a supercritical RD shock wave propagates in an infinite medium, it has $T_- \approx T_1$. If the optical thickness of the unshocked material is not exceedingly small, this is also true in the case of a finite plasma size; the latter applies to all configurations considered in this paper and is directly confirmed by the profiles in figures 3 and 4.

To avoid treatment of the non-planar preheating zone, we make a simplifying assumption that partial deceleration of the infalling plasma in the preheating zone can be neglected, i.e. that one can set $\rho_- = \rho_0$ and $v_- = -(u_\mathrm{s} + U_0)$, where ρ_0 is calculated from (1) at $r = r_\mathrm{s}$, and v_- is the plasma velocity at the entrance into the jump in the shock front frame. As is demonstrated in §16 of chapter VII in [9], for $\gamma - 1 \ll 1$ this approximation is accurate to the second order with respect to the small parameter

$$\eta_{1\infty} = (\gamma - 1)/(\gamma + 1). \tag{21}$$

In fact, it has already been used in condition (19).

Now we can apply equations (15), (16) of mass and momentum balance between the states ρ_-, T_- and ρ_1, T_1:

$$\rho_0 (u_\mathrm{s} + U_0) = \rho_1 |v_1| \equiv j, \tag{22}$$

$$p_- + \rho_0 (u_\mathrm{s} + U_0)^2 = p_1 + \rho_1 v_1^2; \tag{23}$$

here $\rho_0 = \rho_0(r_\mathrm{s})$, and v_1 is the unknown material velocity behind the shock front. Because the shock wave propagates over a falling density profile $\rho_0(r) \propto r^{-1}$, a uniform density distribution behind the front implies that the post-shock density $\rho_1(t)$ decreases with time, and material in the stagnation zone expands. The expansion velocity u is small compared with U_0 but not with the front velocity u_s. As a consequence, we cannot simply put $v_1 = -u_\mathrm{s}$.

By virtue of (22) and (12), equation (23) can be transformed to

$$\eta_1 (1 - \eta_1)(u_\mathrm{s} + U_0)^2 = \frac{p_1}{\rho_1} \left(1 - \eta_1 \frac{T_-}{T_1}\right), \tag{24}$$

where

$$\eta_1 \equiv \frac{\rho_0}{\rho_1} = \frac{|v_1|}{u_\mathrm{s} + U_0} \tag{25}$$

is the inverse of the compression factor. Restricting our treatment to the case of supercritical RD shocks, where $T_- \approx T_1$, we get

$$\eta_1 = \frac{AT_1}{(u_\mathrm{s} + U_0)^2}. \tag{26}$$

In our model η_1 is a small parameter, which is even smaller than the inverse compression factor $\eta_{1\infty}$ in the infinite-media. Keeping this in mind, in all the algebra below we consistently retain only the zeroth and the first terms with respect to this parameter.

A subtle point here is that we cannot directly use equation (17) of the energy balance across the shock front. Quasi-uniform density and temperature profiles in the stagnation core ensue from the rapid redistribution of thermal energy over the entire mass of this zone by means of radiation. Hence, the post-shock thermal energy calculated from the local condition (17) may differ considerably from the required average value. To obtain the latter, we use the condition of global energy balance. For a similar reason, we employ the equation of global mass balance to establish the relationship between the radius r_s and the velocity u_s of the shock front.

The total mass m_s of the compressed core can be expressed as

$$m_\mathrm{s} = m_\mathrm{s}(t) = \pi r_\mathrm{s}^2 \rho_1 = \frac{m_0}{\Delta_0}\,(r_\mathrm{s} + U_0 t)\,, \tag{27}$$

which, by virtue of (25) and (1), yields

$$r_\mathrm{s} = \frac{2\eta_1}{1 - 2\eta_1}\,U_0 t. \tag{28}$$

Since η_1 varies only slowly with time (this can be verified a posteriori), equation (28) implies

$$u_\mathrm{s} \equiv \frac{\mathrm{d}r_\mathrm{s}}{\mathrm{d}t} = \frac{2\eta_1}{1 - 2\eta_1}\,U_0, \qquad r_\mathrm{s} = u_\mathrm{s} t. \tag{29}$$

Combining equations (29) and (26) and omitting the second and higher order terms with respect to η_1, we obtain

$$\eta_1 = \frac{AT_1}{U_0^2 + 4AT_1}, \qquad \frac{u_\mathrm{s}}{U_0} = \frac{2AT_1}{U_0^2 + 2AT_1}. \tag{30}$$

The global energy balance for the imploding plasma mass can be expressed as

$$P_\mathrm{X} + \frac{\mathrm{d}}{\mathrm{d}t}\left[m_\mathrm{s}\epsilon_1 + (m_0 - m_\mathrm{s})\frac{U_0^2}{2}\right] = 0, \tag{31}$$

where P_X is the total (per unit cylinder length) power of x-ray emission, which escapes through the outer boundary. If $P_\mathrm{X} = 0$, we obtain a simple "conservative" result

$$\epsilon_1 = \frac{1}{2}\,U_0^2, \tag{32}$$

which yields

$$T_1 = T_{1\infty} = \frac{\gamma - 1}{2A}\,U_0^2 = \begin{cases} 1.8 \text{ keV} & \text{in case A,} \\ 1.3 \text{ keV} & \text{in case Z.} \end{cases} \tag{33}$$

When equation (32) is used with the realistic equation of state of tungsten, provided by the THERMOS code, it yields $T_{1\infty} \approx 0.8$ keV in case A, and $T_{1\infty} \approx 0.95$ keV

in case Z. It is this post-shock temperature that one would calculate, having literally applied the Raizer's model to a planar stagnation shock in an infinite medium. In our non-conservative situation, where most of the radiation flux escapes the imploding plasma, the final post-shock temperature T_1 is significantly lower than $T_{1\infty}$.

To close up our analytical model, we need an expression for $P_{\rm X}$. If we assume the unshocked infalling plasma to be transparent for the outgoing radiation, we can write

$$P_{\rm X} = 2\pi r_{\rm s}\,\sigma T_1^4, \tag{34}$$

which means that the opaque compressed core of radius $r_{\rm s}$ radiates as a black body with a surface temperature T_1. Clearly, such a situation should correspond to sufficiently small values of m_0, and our case A, as will be seen below, falls into this category.

An additional approximation that we make when opening the brackets in (31) is neglect of the term $m_{\rm s}{\rm d}\epsilon_1/{\rm d}t$ compared to $\epsilon_1{\rm d}m_{\rm s}/{\rm d}t$: this spares us the need to solve a differential equation with practically no loss of accuracy. As a result, upon substitution of (27), (29), (30 and (34) into (31), we arrive at the following equation for determination of $T_1 = T_{1*} = T_{1*}(t)$

$$T_{1*}\left[1 + 4\pi(\gamma-1)\left(\frac{\Delta_0}{m_0}\right)\frac{\sigma T_{1*}^4}{U_0^2 + 4AT_{1*}}\,t\right] = T_{1\infty}, \tag{35}$$

where $T_{1\infty}$ is given by (33). Here we introduced a separate notation T_{1*} for the post-shock temperature T_1, calculated from (35) in the optically thin approximation for the pre-shock plasma, when expression (34) is applied. Having found $T_1 = T_{1*}$ from (35), we calculate η_1, $u_{\rm s}$, $r_{\rm s}$ and ρ_1 from equations (30), (29) and (25), respectively, and this completes our analytical model for the plasma parameters in the stagnation core.

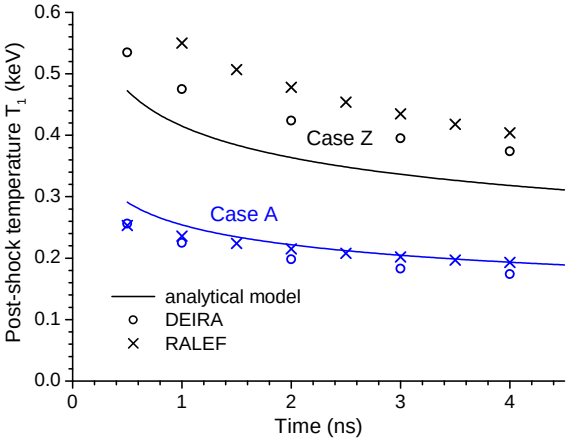

Figure 6. (Colour online) Time dependence of the post-shock temperature T_1: solution of equation (35) $T_1 = T_{1*} = T_{1*}(t)$ (solid curves) is compared with the results of the DEIRA (open circles) and the RALEF (crosses) simulations.

Figure 6 compares the values of $T_1 = T_{1*}$, calculated from equation (35), with those obtained in the DEIRA and RALEF simulations. A very good agreement is observed in case A, where the optical thickness $\tau_{\rm s}$ of the pre-shock plasma at different frequencies has

moderate values around 1 (see figure 16 below). The agreement becomes worse in case Z, where τ_s reaches values around 10 and higher (see figure 19 below): then equation (34) significantly overestimates the radiative energy loss. From the above analysis it follows that the true value of T_1 should be in the range $T_{1*} < T_1 < T_{1\infty}$; when $\tau_s > 1$ increases, the difference $T_1 - T_{1*}$ grows and T_1 approaches the limiting value of $T_1 = T_{1\infty}$. Note that, when considered as a function of the total imploding mass m_0 at a fixed value of U_0, the post-shock temperature T_1 grows with m_0 firstly because T_{1*} increases [as it follows from (35)], and, secondly, because the difference $T_1 - T_{1*} > 0$ becomes larger for $\tau_s \gg 1$.

4.2.3. Temperature peak in the shock front In addition to the post-shock parameters, one would like to have an estimate for the peak matter (electron) temperature T_p inside the shock front (see figures 3 and 4), which defines the hard component of the emitted x-ray spectrum. Such an estimate, however, cannot be obtained without a proper account for thermal conduction. With the conduction energy flux given by

$$S_e = -\kappa \frac{\partial T}{\partial r}, \tag{36}$$

where κ is the conduction coefficient, the temperature T becomes a continuous function across the density jump, while S_e is discontinuous; the radiation energy flux S_r, on the contrary, is everywhere continuous [9]. A qualitative view of the density, temperature and the energy flux profiles across a supercritical RD shock front with strong thermal conduction is shown in figure 7.

In the shock structure shown in figure 7 one can identify four hydrodynamic states: state 0 at the foot of the conduction-preheated layer before the density jump, state "−" at the entrance into the density jump, state "+" upon the exit from the density jump, and state 1 behind the post-shock relaxation zone. The effective width (FWHM) of the conduction-preheated layer is h_-; the effective width of the post-shock relaxation layer is h_+; the effective width of the entire shock front is the sum of the two,

$$\Delta r_s = h_- + h_+. \tag{37}$$

In our case h_- is determined primarily by thermal conduction, whereas for h_+ both the radiant emissivity and thermal conduction are important. Because h_- is much shorter than the shock radius r_s, we can assume that the state 0 lies at the end of the broad radiation-preheating zone and, as in the previous subsection, ignore partial plasma compression and deceleration in the latter. Then, the plasma parameters in the four mentioned states can be represented as in table 1. The parameters in states 0 and 1 are known from the previous subsection. Here we have to evaluate h_-, h_+ and T_p.

We derive a system of approximate equations for the three unknowns h_-, h_+ and T_p by successively applying the general equations (16), (17) of momentum and energy balance three times, for transitions between states 0 and "−", between states "−" and "+", and between states "+" and 1. For each of the three transitions we define a

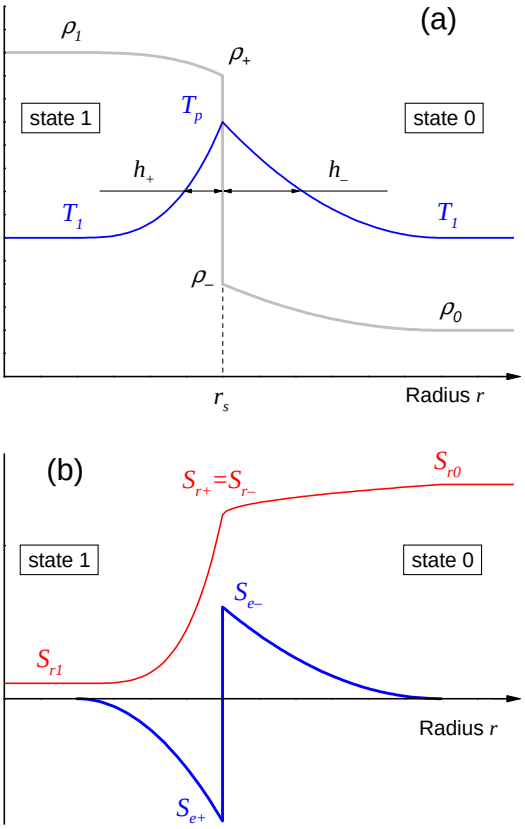

Figure 7. (Colour online) Schematic view of the structure of a supercritical RD shock front with non-zero thermal conduction and zero viscosity. Shown are the density, ρ, and the temperature, T, profiles (a), as well as the profiles of the conductive, S_e, and the radiative, S_r, energy fluxes (b). At $r = r_\mathrm{s}$ the density ρ and the conductive flux S_e are discontinuous.

Table 1. Plasma parameters at four characteristic states inside the RD shock front.

	0	"−"	"+"	1
v	$v_0 = -(u_\mathrm{s} + U_0)$	$v_- = v_0\eta_-$	$v_+ = v_1/\eta_+$	v_1
ρ	$\rho_0 = \rho_0(r_\mathrm{s})$	$\rho_- = \rho_0/\eta_-$	$\rho_+ = \rho_1\eta_+$	ρ_1
T	T_1	T_p	T_p	T_1
S_e	0	$S_{\mathrm{e}-}$	$S_{\mathrm{e}+}$	0
S_r	$S_{\mathrm{r}0}$	$S_{\mathrm{r}-} = S_{\mathrm{r}+}$	$S_{\mathrm{r}+} = S_{\mathrm{r}-}$	$S_{\mathrm{r}1}$

corresponding inverse compression factor

$$\eta_- \equiv \frac{\rho_0}{\rho_-}, \qquad \eta_\mathrm{s} \equiv \frac{\rho_-}{\rho_+}, \qquad \eta_+ \equiv \frac{\rho_+}{\rho_1}; \tag{38}$$

evidently, we must have

$$\eta_-\eta_\mathrm{s}\eta_+ = \eta_1. \tag{39}$$

For the first transition between states 0 and "−" we can neglect the coupling between radiation and matter because here the plasma density $\rho \simeq \rho_0$ is low compared

to the compressed state. The latter means that $S_{\rm r0} \approx S_{\rm r-}$, and equations (16), (17) can be written as

$$A(T_{\rm p} - T_1\eta_-) = \eta_-(1-\eta_-)\,v_0^2, \tag{40}$$

$$\frac{S_{\rm e-}}{j} = \frac{A\gamma}{\gamma-1}(T_{\rm p}-T_1) - \frac{v_0^2}{2}(1-\eta_-^2). \tag{41}$$

Because $T_{\rm p} - T_1 \lesssim T_1$, we have $1-\eta_- \ll 1$, which enables us to reduce equations (40) and (41) to

$$1-\eta_- \approx A(T_{\rm p}-T_1)/v_0^2, \tag{42}$$

$$\frac{S_{\rm e-}}{j} \approx \frac{A}{\gamma-1}(T_{\rm p}-T_1). \tag{43}$$

The second transition is an isothermal density jump between states "−" and "+", where $S_{\rm r}$ is continuous and $S_{\rm e}$ jumps from $S_{\rm e-}$ to $S_{\rm e+}$. Here equations (16), (17) take the form

$$AT_{\rm p} = \eta_{\rm s} v_-^2 = \eta_{\rm s}\eta_-^2 v_0^2, \tag{44}$$

$$\frac{S_{\rm e+}}{j} = \frac{S_{\rm e-}}{j} - \frac{v_-^2}{2}(1-\eta_{\rm s}^2). \tag{45}$$

Neglecting the second and higher order terms with respect to the small parameters $\eta_{\rm s}$ and $1-\eta_-$ in (45), we find

$$\frac{S_{\rm e+}}{j} \approx \frac{A\gamma}{\gamma-1}(T_{\rm p}-T_1) - \frac{v_0^2}{2}. \tag{46}$$

The third transition from state "+" to state 1 occurs in the compressed state, where the plasma emissivity (roughly proportional to the density ρ) is high, and we have to account for variation of the radiation energy flux $S_{\rm r}$. Hence, equations (16), (17) take the form

$$A(T_1 - \eta_+ T_{\rm p}) = \eta_1^2 v_0^2(\eta_+^{-1} - 1), \tag{47}$$

$$\frac{S_{\rm r+} - S_{\rm r1}}{j} = \frac{A\gamma}{\gamma-1}(T_{\rm p}-T_1) + \frac{1}{2}\,\eta_1^2 v_0^2\left(\eta_+^{-2}-1\right) - \frac{S_{\rm e+}}{j}. \tag{48}$$

Retaining just the leading terms with respect to the small parameter η_1, we obtain

$$\eta_+ \approx T_1/T_{\rm p} \quad \Leftrightarrow \quad \rho_1 T_1 \approx \rho_+ T_{\rm p}, \tag{49}$$

$$S_{\rm r+} - S_{\rm r1} \approx \frac{1}{2}\,j v_0^2 \approx \frac{1}{2}\,j U_0^2. \tag{50}$$

As a final step, we express the heat conduction fluxes in terms of the corresponding temperature gradients,

$$S_{\rm e-} \approx \kappa_- \frac{T_{\rm p}-T_1}{2h_-}, \qquad S_{\rm e+} \approx -\kappa_+ \frac{T_{\rm p}-T_1}{2h_+}, \tag{51}$$

and the radiation flux increment

$$S_{\rm r+} - S_{\rm r1} \approx \frac{8}{5}\,\sigma k_{\rm Pl} h_+ \left(T_{\rm p}^4 - T_1^4\right) \tag{52}$$

in terms of the post-shock plasma emissivity; in (51) κ_- and κ_+ are, respectively, the conduction coefficients in states "−" and "+"; in (52) $k_{\rm Pl}$ is the Planckian mean

absorption coefficient of radiation in state "+". Expression (52) is an approximation to the emission power of an optically thin planar layer, which is valid in both limits of $T_\mathrm{p} \gg T_\mathrm{r} = T_1$ and $T_\mathrm{p} \to T_\mathrm{r} = T_1$; the factor $\frac{8}{5}\sigma$ instead of 4σ takes into account that h_+ is the halfwidth of the T rather than the T^4 profile. From (43), (46), (50)–(52) we obtain the following system of three equations for evaluation of h_-, h_+ and T_p:

$$h_- = (\gamma - 1)\kappa_-/(2jA), \tag{53}$$

$$h_+ = \frac{5}{16}\frac{jU_0^2}{\sigma k_\mathrm{Pl}(T_\mathrm{p}^4 - T_1^4)}, \tag{54}$$

$$\frac{jU_0^2}{T_\mathrm{p} - T_1} = \frac{\kappa_+}{h_+} + \frac{2jA\gamma}{\gamma - 1}. \tag{55}$$

For numerical estimates we use power-law approximations

$$\kappa_- \approx \kappa_+ \approx 0.15\, T_\mathrm{p,keV}^2 \text{ TW cm}^{-1} \text{ keV}^{-1}, \tag{56}$$

$$k_\mathrm{Pl} \approx 700\, \frac{\rho_\mathrm{+,g/cc}}{T_\mathrm{p,keV}} \approx 700\, \frac{\rho_\mathrm{1,g/cc} T_\mathrm{1,keV}}{T_\mathrm{p,keV}^2} \text{ cm}^{-1}, \tag{57}$$

to the THERMOS data for tungsten in the relevant parameter range.

Table 2. Comparison of the analytically evaluated stagnation shock parameters with the RALEF results.

	case A, $t = 3$ ns		case Z, $t = 3$ ns	
	analytical	RALEF	analytical	RALEF
ρ_1 (g cm^{-3})	4.0	3.5	14.2	7.3
T_1 (keV)	0.205	0.20	0.34	0.44
T_p (keV)	0.406	0.35	0.65	0.54
Δr_s (μm)	1.2	0.8	0.3	< 0.4
h_- (μm)	1.08	—	0.24	—
h_+ (μm)	0.14	—	0.08	—

In table 2 the analytically evaluated shock parameters are compared with those obtained in the RALEF simulations for $t = 3$ ns. Generally, the analytical model tends to produce higher values of the peak temperature T_p than the DEIRA and the RALEF codes because of an assumed sharp angle in the temperature profile (see figure 7), which is smeared either by artificial viscosity in the DEIRA code, or by insufficient spatial resolution in the RALEF simulations. It is clearly seen that, as one passes from case A to a more powerful case Z, the stagnation shock becomes significantly hotter and more narrow — in full agreement with general properties of supercritical RD shocks [9]. Because of the intricate coupling between thermal conduction and radiation emission, no universal power-law scaling for T_p and Δr_s can be deduced from (53)-(57).

5. X-ray pulse

The 3T model of the DEIRA code is reasonably adequate for calculating the total power profile of the x-ray pulse (see figures 8 and 9 below), but can provide no information on its spectral characteristics. For this one has to solve the equation of spectral radiation transfer together with the hydrodynamics equations, and that is where we employ the RALEF-2D code.

5.1. Power profile

Figures 8 and 9 show the temporal x-ray power profiles $P_{\rm X} = P_{\rm X}(t)$ as calculated with the DEIRA and the RALEF codes, which agree fairly well with one another, especially in case A. These profiles demonstrate a clear quasi-steady phase, which lasts about 4 ns in case A, and about 2.5 ns in case Z; at this phase $P_{\rm X}$ is close to the nominal power P_0. A marked difference between cases A and Z is a later (by $\simeq 1$ ns) rise of the x-ray power in case Z. This delay occurs because in case Z the radiation heat wave has to propagate through a more massive and optically thick layer of cold plasma before it breaks out to the surface. The overall efficiency of conversion of the initial kinetic energy into radiation (by $t = 6$ ns) is 92% in case A and 78% in case Z according to the RALEF data, and 94% in case A and 81% in case Z according to the DEIRA results.

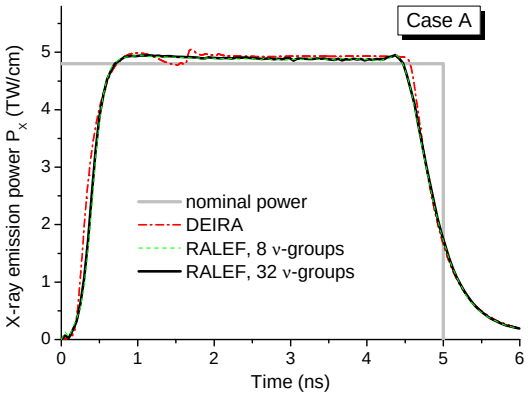

Figure 8. (Colour online) Temporal profile of the total x-ray emission power $P_{\rm X}$ in case A: the results of three different numerical simulations are compared among themselves and with the nominal power profile, which corresponds to an instantaneous 100% conversion of the plasma kinetic energy into x-ray emission.

The flat-top shape of the $P_{\rm X}(t)$ profiles in figures 8 and 9 is a direct consequence of the $\rho_0(r) \propto r^{-1}$ initial density profile (1), which, for a constant implosion velocity $u(r) = -U_0$, implies the simplest box-like profile of the nominal power $P_0(t) = -{\rm d}E_{\rm kin}/{\rm d}t$ of the kinetic energy dissipation. Our simulations demonstrate that in relatively low-mass implosions, where the effective optical thickness of the infalling plasma is $\lesssim 1$, the observed x-ray pulse closely mimics the nominal power profile, which for cold implosions is directly related to the density and velocity profiles at the time of shell collapse. In such a case the observed x-ray pulse might to a good accuracy be represented as a

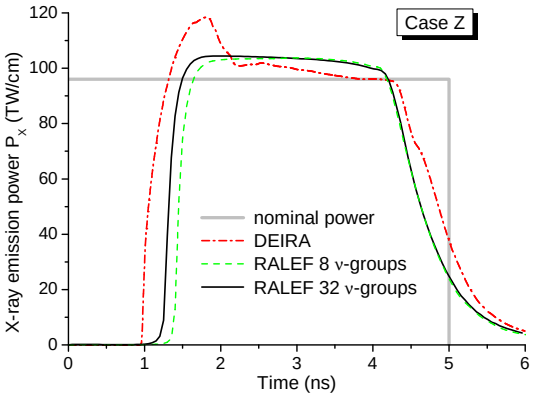

Figure 9. (Colour online) Same as figure 8 but in case Z.

superposition of subpulses, generated by different layers of the imploding shell that arrive successively at the stagnation shock front. Hence, the observed pulse shape can be easily fitted by a corresponding adjustment of the ρ and u profiles. However, in high-mass implosions (like in case Z) the relation between the nominal and the observed power profiles is more complex because of the reabsorption of the primary x-rays in the optically thick infalling plasma. Generally, if the imploding shell is relatively cold and optically thick, and generates a smooth nominal power profile, our model would predict a significant steepening of the rising edge of the observed pulse due to a sudden radiation wave breakout.

5.2. Shock structure in the RALEF simulations

Radial density and temperature profiles in the imploding plasma, obtained with the RALEF code, are shown in figures 10 and 11. Despite quite different physical models, the RALEF and the DEIRA results agree almost perfectly in case A: we calculate practically the same values of the post-shock, T_1, and the peak, T_p, matter temperatures. Figure 10 also demonstrates that in case A the temperature peak is fairly well resolved in 2D simulations, although appears somewhat broader than in the 1D DEIRA picture. Larger 2D values of the shock radius r_s are explained by different position of the inner boundary (at $r = 10$ μm in the 2D case versus $r = 0$ in the 1D case).

In case Z, on the contrary, the temperature peak is rather poorly resolved in 2D simulations, as one sees in figure 11 — despite a larger total number of radial mesh zones (600 in case Z versus 250 in case A). The reason is twofold: on the one hand, the temperature peak in case Z is about a factor 2 more narrow than in case A; on the other, a considerably larger shock radius r_s causes the RALEF mesh rezoning algorithm to force a coarser grid along the radial direction. Nevertheless, the agreement between the RALEF and the DEIRA results for the post-shock, T_1, and the peak, T_p, matter temperatures is also fairly good.

Radial profiles of the implosion velocity $-u(r)$ at $t = 3$ ns are displayed in figure 12 for both cases A and Z. One notices that the fluid velocity changes sign across the shock

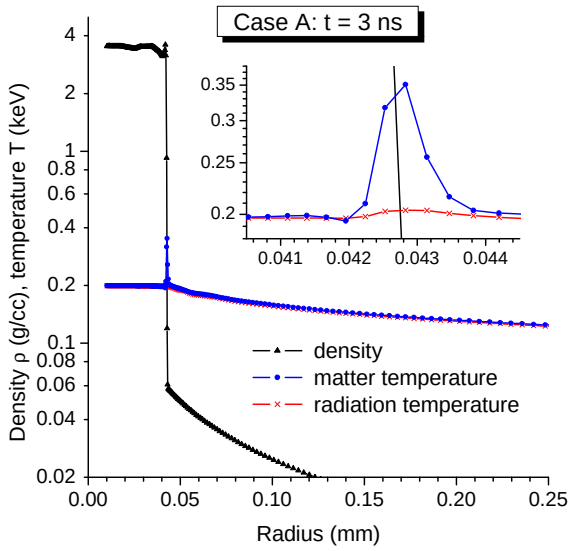

Figure 10. (Colour online) Radial density and temperature profiles at $t = 3$ ns in case A obtained in the 2D RALEF simulation with 32 spectral groups.

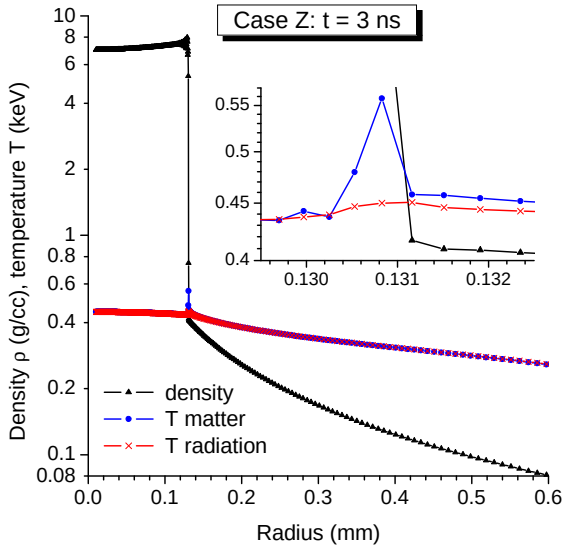

Figure 11. (Colour online) Same as figure 10 but in case Z.

front. As was already mentioned in section 4.2.2, the post-shock plasma on average slowly expands (i.e. has a negative implosion velocity) because the stagnation shock propagates over a falling density profile. Near the outer edge, the infalling plasma has already been significantly decelerated, especially in the more massive case Z. The decelerating pressure gradient is created by re-deposition of radiant energy transported from the stagnation shock front.

Figure 13 shows spatial profiles of the mean ion charge $z_{\rm ion}$ at $t = 3$ ns. One sees that tungsten ions with charges of $z_{\rm ion} = 40$–45 are present inside the stagnation shock front. It should be reminded here that these ion charges have been calculated in the LTE limit. A direct evidence that the LTE approximation is quite adequate in

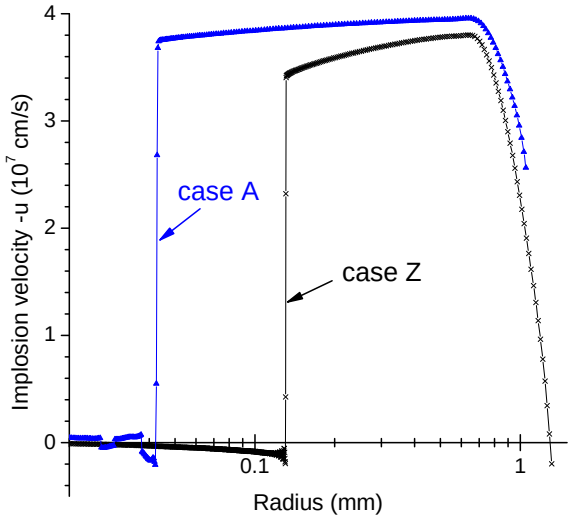

Figure 12. (Colour online) Radial profiles of the plasma implosion velocity (minus the radial velocity u) at $t = 3$ ns in cases A and Z as calculated by the RALEF code with 32 spectral groups. Logarithmic scale for the radius allows to show the detailed structure of the compact shocked region together with the overall large scale behaviour.

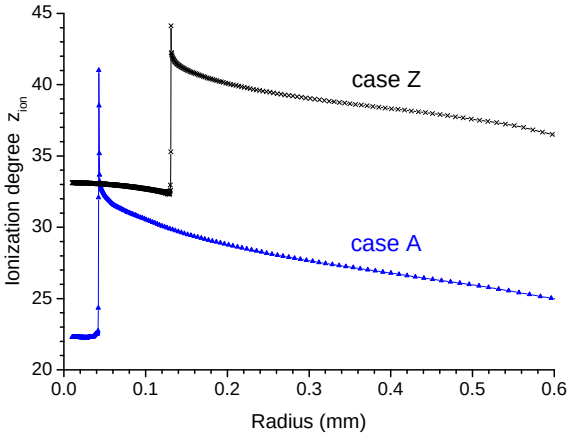

Figure 13. (Colour online) Radial profiles of the tungsten ionization degree $z_{\rm ion}$ at $t = 3$ ns in cases A and Z as calculated by the RALEF code with 32 spectral groups in the radiation transport module.

our situation is a close agreement between the radiation and matter temperatures in figures 10 and 11. The applicability of LTE can only be questioned inside the narrow shock front. However, the plasma density there is already so high ($n_{\rm e} \gtrsim 6 \times 10^{21}$ in case A, and $n_{\rm e} \gtrsim 5 \times 10^{22}$ in case Z) that non-LTE corrections to the values of $z_{\rm ion}$ and T inside the shock front are not expected to be significant (poor spatial resolution of this region may, in fact, be a no less important issue).

5.3. Spatially integrated spectra

5.3.1. Case A The overall x-ray spectrum emitted by the imploding pinch in case A at $t = 3$ ns is shown in two different representations in figures 14 and 15. This spectrum would have been observed through an imaginary slit perpendicular to the pinch axis by a detector without spatial resolution. More precisely, figures 14 and 15 display the spectral power F_ν [TW cm^{-1} sr^{-1} keV^{-1}] per unit cylinder length, obtained by integrating along the slit the intensity $I_\nu(\mathbf{\Omega})$ of the outgoing radiation, which propagates in direction $\mathbf{\Omega}$ perpendicular to the pinch axis. The shown spectrum was obtained by solving the transfer equation (7) in the post-processor mode for 200 spectral groups of the secondary frequency set. In case A it turns out to be rather insensitive to the number of spectral groups (either 8 or 32) coupled to the hydrodynamics energy equation.

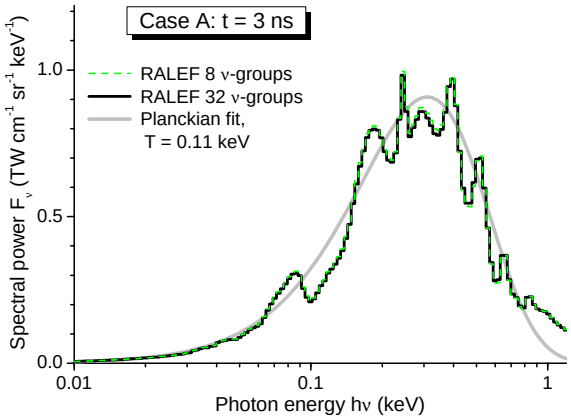

Figure 14. (Colour online) Spectral power of x-ray emission per unit cylinder length at $t = 3$ ns in case A: the soft part of the x-ray spectrum. The Planckian-fit curve is normalized to the emission peak.

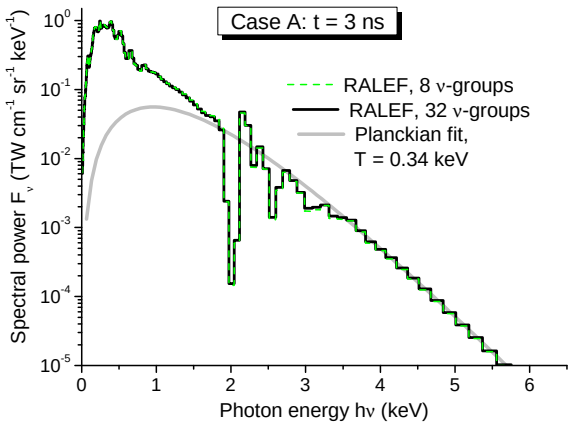

Figure 15. (Colour online) Spectral power of x-ray emission per unit cylinder length $t = 3$ ns in case A: the hard part of the x-ray spectrum. The Planckian-fit curve is normalized to the $h\nu \gtrsim 3$ keV tail of the emission.

The plots in figures 14 and 15 demonstrate that the emitted spectrum can roughly

be approximated as a superposition of two Planckian curves: one with a temperature $T_{\rm r1} \approx 0.11$ keV, and the other with a temperature $T_{\rm r2} \approx 0.34$ keV. The interpretation of the hard component is straightforward: it is the thermal emission of the temperature peak $T_{\rm p} = T_{\rm ep} \approx T_{\rm r2}$ inside the stagnation shock. In our case this component carries about 16% of the total x-ray flux and is emitted by an optically thin plasma layer rather than by a surface of a black body.

The soft component originates from a much broader halo around the shock front, at an effective radius of $r_{\rm em} \approx 0.4$ mm $\gg r_{\rm s} = 0.043$ mm. This halo is the result of reprocession of the original shock emission by the cold layers of the unshocked material. Note that the temperature $T_{\rm r1}$ of the soft component is significantly lower than the post-shock matter temperature $T_1 = 0.20$ keV, which implies that even in the low-mass case A the infalling unshocked plasma is not truly optically thin.

Figure 16 provides more detailed information on the radial profiles of the spectral optical depth. It is seen that, depending on the photon energy, the optical thickness of the unshocked plasma can be either significantly below or significantly above unity. The latter means that the effective emitting layer is, in fact, not well defined, and the observed spectrum may exhibit significant deviations from the Planckian shape. Indeed, a number of prominent dips and spikes in the calculated spectrum in figures 14 and 15 arise as a combined effect of a complex spectral dependence of the tungsten opacity, shown in figure 1, superimposed on a nontrivial temperature distribution inside and above the stagnation shock.

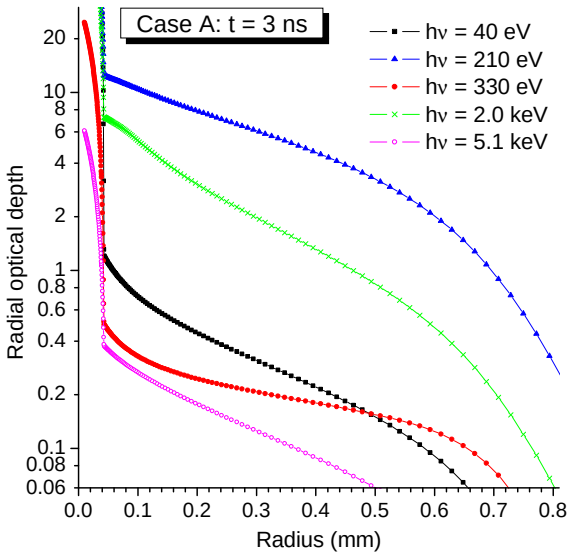

Figure 16. (Colour online) Profiles of radial optical thickness at different photon energies for $t = 3$ ns in case A.

5.3.2. Case Z Figures 17 and 18 display the same information as figures 14 and 15 but for a 20 times larger (6 mg cm^{-1}) imploding mass of case Z. Here both the main component of the spectrum in figure 17 and the hard component in figure 18

correspond to roughly two times higher Planckian-fit temperatures of $T_{r1} = 0.21$ keV and $T_{r2} = 0.53$ keV; the hard component carries about 7% of the total x-ray flux.

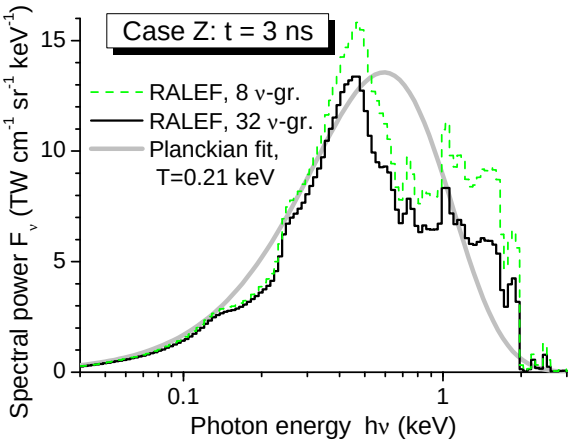

Figure 17. (Colour online) Same as figure 14 but for case Z.

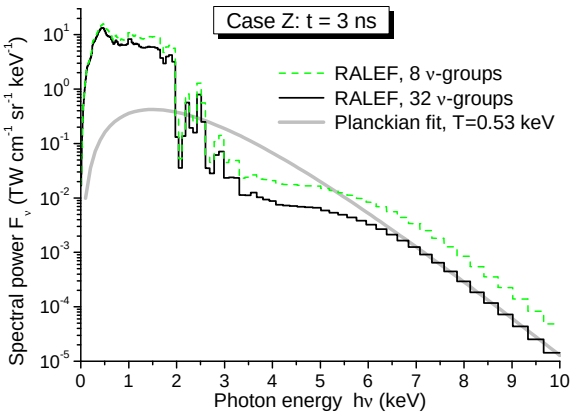

Figure 18. (Colour online) Same as figure 15 but for case Z. The Planckian-fit curve is normalized to the $h\nu \gtrsim 6$ keV tail of the emission.

In contrast to case A, now the shock front lies at an optical depth τ_s well in excess of unity at all frequencies: as can be seen in figure 19, at $t = 3$ ns the optical depth τ_s varies in the range $\tau_s \approx 4$–100. As a result, the calculated spectrum in figures 17 and 18 demonstrates higher sensitivity to the number of spectral groups coupled to hydrodynamics. The effective emission radius for the equivalent Planckian flux can be evaluated as $r_{em} \approx 0.7$ mm. Figure 19 shows that it is around this radius that the spectral optical depth is on the order of unity.

Our calculated spectrum in figure 18 appears to be in fair agreement with the observed x-ray spectra for 6 mg cm^{-1} tungsten arrays tested on the Z machine [11, 4], although the published experimental data at $h\nu \gtrsim 3$–4 keV are rather scarce. In fact, when we superpose our spectrum in figure 18 on that from [31], we observe a very good agreement without even rescaling the absolute fluxes. The experimental points for

$h\nu > 2$ keV, quoted in [4, 31], do indicate the presence of a hard x-ray component with an effective temperature of $T_{\rm r2} \approx 0.6$ keV, whereas the main emission is reasonably well approximated by a blackbody spectrum with $T_{\rm r1} \approx 165$ eV [31]. Note that, according to our results, particularly in the region $h\nu = 3$–6 keV, the spectral slope appears to be significantly flattened as compared to the corresponding Planckian fit of the hard component — which implies complications for any direct interpretation of the Planckian-fit temperature, inferred from the experimental data in this region.

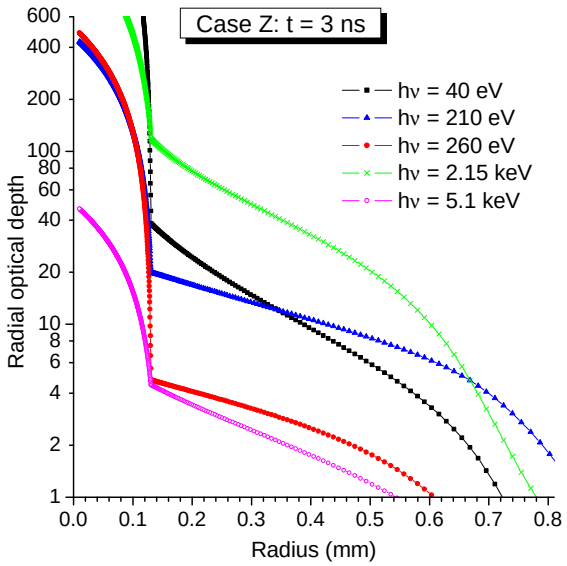

Figure 19. (Colour online) Same as figure 16 but for case Z.

5.4. Calculated 1D x-ray images

Beside spatially integrated emission spectra, of certain interest might be theoretical spectral images of the imploding pinch. A selection of such images is shown in figures 20 and 21 for the time $t = 3$ ns. Here the radiation intensity $I_\nu = I_\nu(s, \mathbf{\Omega})$ is plotted as a function of distance along an imaginary observation slit, perpendicular to the pinch axis, as it would be registered by an observer at infinity; the photon propagation direction $\mathbf{\Omega}$ is also perpendicular the pinch axis. Again, these images have been constructed in the post-processor mode by separate integration of the transfer equation (7) along a predefined set of rays (long characteristics) at selected photon energies. This enabled us to get rid of the numerical diffusion inherent in the method of short characteristics.

Our principal motivation for presenting the images in figures 20 and 21 was to illustrate how one could possibly resolve the RD shock front around the stagnant plasma core, buried deeply inside the imploding plasma column. Figure 20 demonstrates that in the low-mass case A this could already be achieved by radiography at photon energies around $h\nu \approx 2$ keV. In the more massive case Z one has to do the measurements in harder x-rays at $h\nu \gtrsim 8$ keV. The softer part of the spectrum reveals only a broad blurred halo from the imploding plasma, whose size depends on the observation frequency.

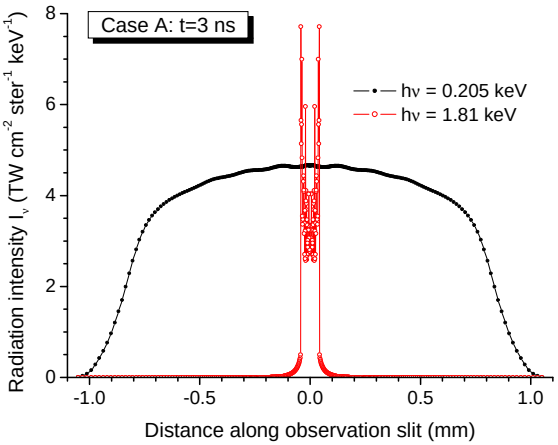

Figure 20. (Colour online) 1D x-ray image of the imploding pinch at two different frequencies in case A at $t = 3$ ns.

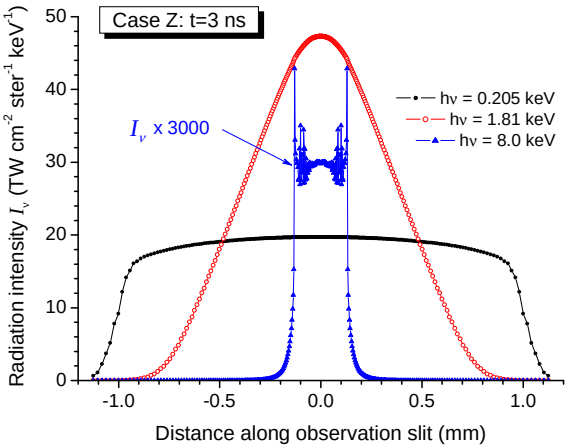

Figure 21. (Colour online) Same as figure 20 but for case Z and three different frequencies.

In three dimensions, with realistic flow non-uniformities, the dense and opaque stagnant plasma "core" will certainly have a more intricate shape than a simple cylindrical column, for which our present analysis can provide no clues. The 1D images in figures 20 and 21 suggest that the stagnant core can only be resolved at sufficiently high photon energies of several keV — the threshold depending on the total imploding mass. In reality such an image may look similar to the one obtained at $h\nu = 6.15$ keV in one of the Sandia shots [32, figure 5]. Our simulations indicate that typical sizes of structures to be observed should fall in the range of 100–300 μm for tungsten pinches with masses 0.3–6 mg/cm. Also, our model implies that, having become visible at a certain frequency, the radiographic image of the dense stagnant plasma should preserve its shape and size with further increase of the observation frequency.

6. Summary

In this work, within the framework of pure radiation hydrodynamics, we have attempted to present a detailed physical picture of how the kinetic energy of the imploding high-Z (tungsten) plasma in wire array z-pinches could be converted into powerful bursts of x-rays. Having concentrated on a self-consistent modelling of the emergent x-ray spectra, we adopted the simplest possible formulation of the problem. In particular, we assumed that at the final stage of kinetic energy dissipation the dynamic effects due to the magnetic field could be neglected, and that the imploding tungsten plasma has a perfectly symmetric one-dimensional cylindrical configuration. Both assumptions imply severe idealization of the problem, and how realistic are the conclusions reached under them, remains to be clarified by future work.

The reason for our 1D statement of the problem is simply because the 1D picture is always a necessary starting point when exploring a complex physical phenomenon: later on it may serve as a valuable reference case — especially if it manages to capture the basic physical features of the studied phenomenon.

However, even if we skip the initial phase of plasma acceleration by the $\mathbf{j} \times \mathbf{B}$ force and stay within the 1D picture, there remains a question of possible dynamic and kinetic effects due to the (partially) frozen-in magnetic field. We do not expect that such effects can significantly alter the present physical picture of the x-ray pulse formation (at least not in the phase of what we call the main x-ray pulse) simply because the initial Alfvenic Mach number is very high ($\gtrsim 40$). Later on, as the bulk of the imploding mass passes through the stagnation shock and the pinch enters the stagnation phase with a Bennet-type equilibrium, the effects due to the magnetic field and the ensuing MHD instabilities may, of course, become much more significant. This second phase of the x-ray pulse, which may in fact account for a large portion of the total emitted x-ray energy and be strongly dominated by the MHD effects, was not the topic of our present work.

Within the approximations made, we have demonstrated that the conversion of the implosion energy into quasi-thermal x-rays occurs in a very narrow (sub-micron) radiation-dominated shock front, namely, in an RD stagnation shock with a supercritical amplitude according to the classification of [9]. We analyzed the structure of the stagnation RD shock by using two independent radiation-hydrodynamics codes, and by constructing an approximate analytical model.

We have found that the x-ray spectrum, calculated with the 2D RALEF code by solving the equation of spectral radiative transfer in the imploding plasma, agrees fairly well with the published experimental data for the 6 mg cm^{-1} tungsten wire arrays tested at Sandia. The hard component of the x-ray spectrum with a blackbody temperature of $T_{\rm r2} \approx 0.5$–0.6 keV is shown to originate from a narrow peak of the electron temperature inside the RD stagnation shock. Our approximate model clarifies how the width and the amplitude of this temperature peak depend on the imploding plasma parameters. A potentially important implication of this result is that 2D and 3D simulations of imploding z-pinches with insufficient spatial resolution for the RD shock front can

hardly be expected to adequately reproduce the hard component of the emergent x-ray spectrum (typically, the peak electron temperature of the emitting layer would be underestimated). The softer main component of the x-ray pulse is generated in an extended halo around the stagnation shock, where the primary emission from the shock front is absorbed and reemitted by the outer layers of the imploding plasma.

Although the analysis in this work has been performed for particular initial density (1) and implosion velocity (constant) profiles, which correspond to the simplest box-like pulse of the nominal power (the power $P_0(t) = \mathrm{d}E_{\mathrm{kin}}/\mathrm{d}t$ of the kinetic energy dissipation in the stagnation shock front), our principal results remain valid for other physically plausible implosion profiles as well. The physical characteristics of the RD shock front and the emergent x-ray spectrum (near the peak of the pulse) are practically uniquely controlled by such global implosion parameters as the total mass $m_0 = 2\pi \int r\rho_0(r)\,\mathrm{d}r$ and kinetic energy $E_0 = \int P_0(t)\,\mathrm{d}t$ of the imploding shell together with the peak value $\max\{P_0(t)\}$ of the nominal power. This conclusion can be inferred from our analysis of the relevant physical processes, and has been directly verified by a separate 2D simulation with the initial density profile

$$\rho_0(r) = \left(\frac{m_0}{2\pi\Delta_0}\right)\frac{1}{r}\sin\left(\frac{2r}{\Delta_0}\right), \qquad 0 \le r \le \frac{\pi}{2}\Delta_0, \tag{58}$$

which, for a constant implosion velocity $u(r) = -U_0$, corresponds to a sine-like profile of the nominal power $P_0(t)$ but yields the peak x-ray spectrum practically identical with the one in figures 17 and 18.

In reality, due to flow non-uniformities, the narrow front of the stagnation shock will almost certainly have a much more irregular shape than in the present 1D picture. But its main characteristics — the transverse thickness Δr_{s} and the peak electron temperature T_{ep} — are controlled by the plasma flow parameters (the implosion velocity U_0, the mass flux density $\rho_0 U_0$, the plasma thermal conductivity κ and the spectral absorption coefficient k_ν) that are not expected to be dramatically affected by moderate flow perturbations. Hence, we expect that radiation-hydrodynamics simulations of realistically perturbed implosions should produce emergent x-ray spectra close to those calculated in the present work.

Acknowledgments

This work was partially supported by the Russian Foundation for Basic Research with grant No. 09-02-01532-a, by the Russian Ministry of Education and Science under contract No. MES-16.518.11.7001, and by the ExtreMe Matter Institute EMMI in the framework of the Helmholtz Alliance Program HA216/EMMI. The authors are also grateful to the two anonymous referees for their constructive and stimulating comments.

References

[1] Spielman R B *et al* 1998 *Phys. Plasmas* **5** 2105

[2] Deeney C *et al* 1998 *Phys. Rev. Lett.* **81** 4883
[3] Matzen M K *et al* 2005 *Phys. Plasmas* **12** 055503
[4] Cuneo M E *et al* 2006 *Plasma Phys. Control. Fusion* **48** R1
[5] Chittenden J P, Lebedev S V, Bland S N, Beg F N and Haines M G 2001 *Phys. Plasmas* **8** 2305
[6] Chittenden J P, Lebedev S V, Jennings C A, Bland S N and Ciardi A 2004 *Plasma Phys. Control. Fusion* **46** B457
[7] Jennings C A *et al* 2010 *Phys. Plasmas* **17** 092703
[8] Stygar W A *et al* 2004 *Phys. Rev.* E **69** 046403
[9] Zel'dovich Ya B and Raizer Yu P 1967 *Physics of Shock-Waves and High-Temperature Hydrodynamic Phenomena* vol II (New York: Academic Press)
[10] Aleksandrov V V *et al* 2004 *Plasma Phys. Rep.* **30** 568
[11] Cuneo M E *et al* 2005 *Phys. Rev* E **71** 046406
[12] Grabovski E V, Zukakishvili G G, Nedoseev S L, Oleinik G M and Porofeev I Yu 2004 *Plasma Phys. Rep.* **30** 30
[13] Grabovski E V *et al* 2006 *Plasma Phys. Rep.* **32** 32
[14] Aleksandrov V V *et al* 2001 *Plasma Phys. Rep.* **27** 89
[15] Yu E P *et al* 2007 *Phys. Plasmas* **14** 022705
[16] Sasorov P V, Oliver B V, Yu E P and Mehlhorn T A 2008 *Phys. Plasmas* **15** 022702
[17] Basko M M 1990 *Nucl. Fusion* **30** 2443
[18] Basko M M 2001 DEIRA: a 1D 3T Hydrodynamic Code for Simulating ICF Targets Driven by Fast Ion Beams. Version 4. http://www.basko.net/mm/deira (unpublished)
[19] Basko M M, Maruhn J and Tauschwitz An 2010 *GSI Scientific Report 2009: GSI Report 2010-1* (Darmstadt, Germany: Gesellschaft für Schwerionenforschung mbH) p 410
[20] Basko M M 1985 *High Temperature* **23** 388
[21] Imshennik V S, Mikhailov I N, Basko M M and Molodtsov S V 1986 *Soviet Phys. JETP* **63** 980
[22] Addessio F L *et al* 1992 CAVEAT: A Computer Code for Fluid Dynamics Problems With Large Distortion and Internal Slip *LA-10613-MS-Rev. 1, UC-32* (Los Alamos: Los Alamos National Laboratory)
[23] Winslow A M 1981 Adaptive Mesh Zoning by the Equipotential Method *UCID-19062* (Livermore: Lawrence Livermore National Laboratory)
[24] Livne E and Glasner A 1985 *J. Comp. Phys.* **58** 59
[25] Basko M M, Maruhn J and Tauschwitz An 2009 *J. Comput. Phys.* **228** 2175
[26] Larsen E W, Morel J E and Miller W F, Jr. 1987 *J. Comp. Phys.* **69** 283
[27] Dedner A and Vollmöller P 2002 *J. Comput. Phys.* **178** 263
[28] Nikiforov A F, Novikov V G and V. B. Uvarov V B 2005 *Quantum-statistical models of hot dense matter: methods for computation of opacity and equation of state* (Basel-Boston-Berlin: Birkhauser Verlag)
[29] Raizer Yu P 1957 *Soviet Phys. JETP* **5** 1242
[30] Zel'dovich Ya B 1957 *Soviet Phys. JETP* **5** 919
[31] Foord M E *et al* 2004 *Phys. Rev. Lett.* **93** 055002
[32] Sinars D B *et al* 2008 *Phys. Rev. Lett.* **100** 145002